

A Super-Earth Orbiting Near the Inner Edge of the Habitable Zone around the M4.5-dwarf Ross 508

Hiroki HAKAWA¹ Takuya TAKARADA^{2,3} Yui KASAGI⁴ Teruyuki HIRANO^{2,3,4} Takayuki KOTANI^{2,3,4} Masayuki KUZUHARA^{2,3} Masashi OMIYA^{2,3}
Hajime KAWAHARA⁵ Akihiko FUKUI⁶ Yasunori HORI^{2,3,4} Hiroyuki Tako ISHIKAWA^{2,3} Masahiro OGIHARA^{7,8,3} John LIVINGSTON^{2,3,9} Timothy D. BRANDT¹⁰ Thayne CURRIE^{1,11,12} Wako AOKI³ Charles A. BEICHMAN^{13,14} Thomas HENNING¹⁵ Klaus HODAPP¹⁶ Masato ISHIZUKA⁹ Hideyuki IZUMIURA¹⁷ Shane JACOBSON¹⁶ Markus JANSON¹⁸ Eiji KAMBE¹ Takanori KODAMA⁶ Eiichiro KOKUBO³ Mihoko KONISHI¹⁹ Vigneshwaran KRISHNAMURTHY^{2,3} Tomoyuki KUDO¹ Takashi KUROKAWA^{2,20} Nobuhiko KUSAKABE^{2,3} Jungmi KWON⁹ Yuji MATSUMOTO³ Michael W. McELWAIN²¹ Koyu MITSUI⁹ Takao NAKAGAWA²² Norio NARITA^{2,6,23} Jun NISHIKAWA^{3,4,2} Stevanus K. NUGROHO^{2,3} Eugene SERABYN²⁴ Takuma SERIZAWA^{20, 3} Aoi TAKAHASHI^{2,3} Akitoshi UEDA^{2,3,4} Taichi UYAMA^{13,14,3} Sébastien VIEVARD^{1,2} Ji WANG²⁵ John WISNIEWSKI²⁶ Motohide TAMURA^{9,2,3} Bun’ei SATO²⁷

¹Subaru Telescope, 650 North A’ohoku Place, Hilo HI 96720, USA

²Astrobiology Center, 2-21-1 Osawa, Mitaka, Tokyo 181-8588, Japan

³National Astronomical Observatory of Japan, 2-21-1 Osawa, Mitaka, Tokyo 181-8588, Japan

⁴Department of Astronomical Science, The Graduate University for Advanced Studies, SOKENDAI, 2-21-1 Osawa, Mitaka, Tokyo 181-8588, Japan

⁵Department of Earth and Planetary Sciences, Graduate School of Science, The University of Tokyo, 7-3-1 Hongo, Bunkyo-ku, Tokyo 113-0033, Japan

⁶Komaba Institute for Science, The University of Tokyo, 3-8-1 Komaba, Meguro, Tokyo 153-8902, Japan

⁷Tsung-Dao Lee Institute, Shanghai Jiao Tong University, 520 Shengrong Road, Shanghai 201210, China

⁸Earth-Life Science Institute, Tokyo Institute of Technology, 2-12-1 Ookayama, Meguro, Tokyo 152-8550, Japan

⁹Department of Astronomy, Graduate School of Science, The University of Tokyo, 7-3-1 Hongo, Bunkyo-ku, Tokyo 113-0033, Japan

¹⁰Department of Physics, University of California, Santa Barbara, Santa Barbara, CA 93106, USA

¹¹NASA-Ames Research Center, Moffett Field, CA, USA

¹²Eureka Scientific, Oakland, 10 CA, USA

¹³Infrared Processing and Analysis Center, California Institute of Technology, 1200 E. California Boulevard, Pasadena, CA 91125, USA

¹⁴NASA Exoplanet Science Institute, Pasadena, CA 91125, USA

¹⁵Max-Planck-Institut für Astronomie, Königstuhl 17, 69117 Heidelberg, Germany

¹⁶University of Hawaii, Institute for Astronomy, 640 N. Aohoku Place, Hilo, HI 96720, USA

¹⁷Okayama Branch, Subaru Telescope, National Astronomical Observatory of Japan, National Institute of Natural Sciences, Kamogata, Asakuchi, Okayama 719-0232, Japan

¹⁸Department of Astronomy, Stockholm University, SE-10691, Stockholm, Sweden

¹⁹Faculty of Science and Technology, Oita University, 700 Dannoharu, Oita 870-1192, Japan

²⁰Institute of Engineering, Tokyo University of Agriculture and Technology, 2-24-16, Nakacho, Koganei, Tokyo, 184-8588, Japan

²¹Exoplanets and Stellar Astrophysics Laboratory, NASA Goddard Space Flight Center, Greenbelt, MD 20771, USA

²²Institute of Space and Astronautical Science, Japan Aerospace Exploration Agency, 3-1-1 Yoshinodai, Chuo-ku, Sagami-hara, Kanagawa 252-5210, Japan

²³Instituto de Astrofísica de Canarias (IAC), 38205 La Laguna, Tenerife, Spain

²⁴Jet Propulsion Laboratory, California Institute of Technology, Pasadena, California 91109, USA

²⁵Department of Astronomy, The Ohio State University, 100 W 18th Ave, Columbus, OH 43210 USA

²⁶Department of Physics and Astronomy, University of Oklahoma, 440 West Brooks Street, Norman, OK 73019, USA

²⁷Department of Earth and Planetary Sciences, Tokyo Institute of Technology, 2-12-1 Ookayama, Meguro-ku, Tokyo 152-8551, Japan

*E-mail: harakawa@naoj.org

Received (March 5, 2022); Accepted (May 23, 2022)

Abstract

We report the near-infrared radial-velocity (RV) discovery of a super-Earth planet on a 10.77-day orbit around the M4.5 dwarf Ross 508 ($J_{\text{mag}} = 9.1$). Using precision RVs from the Subaru Telescope IRD (InfraRed Doppler) instrument, we derive a semi-amplitude of $3.92^{+0.60}_{-0.58} \text{ m s}^{-1}$, corresponding to a planet with a minimum mass $m \sin i = 4.00^{+0.53}_{-0.55} M_{\oplus}$. We find no evidence of significant signals at the detected period in spectroscopic stellar activity indicators or MEarth photometry. The planet, Ross 508 b, has a semimajor-axis of $0.05366^{+0.00056}_{-0.00049} \text{ au}$. This gives an orbit-averaged insolation of ≈ 1.4 times the Earth's value, placing Ross 508 b near the inner edge of its star's habitable zone. We have explored the possibility that the planet has a high eccentricity and its host is accompanied by an additional unconfirmed companion on a wide orbit. Our discovery demonstrates that the near-infrared RV search can play a crucial role to find a low-mass planet around cool M dwarfs like Ross 508.

Key words: infrared: planetary systems — planets and satellites: terrestrial planets — techniques: radial velocities

1 Introduction

Since the discovery of 51 Pegasi b around a solar-type star (Mayor & Queloz 1995), precision radial velocity (RV) searches have discovered nearly a thousand exoplanets (Schneider et al. 2011). More recently, transit surveys, with observatories including *CoRoT* (Baglin et al. 2006), *Kepler* (Borucki et al. 2010), and *TESS* (Ricker et al. 2015) have discovered several thousand more. Exoplanets are known to orbit various types of stars such as solar-type stars (e.g. Lissauer et al. 2011), low-mass M dwarfs (Gillon

et al. 2017), evolved stars (Teng et al. 2022), and stellar remnants (e.g. Vanderburg et al. 2020). Among them, M-type stars are especially promising targets for the detection of Earth-like planets. These stars' small sizes make transits relatively deep, and their low luminosities make the habitable zone close to the star where the RV amplitude is larger.

Nevertheless, exoplanet discoveries around cool M dwarfs are still limited.¹ Most exoplanet surveys have used optical CCDs in their cameras but such cool stars

¹ Only 3 (2) stars with effective temperatures less than 3000 K have been

emit most of their energy in the near-infrared (NIR). One of the most effective ways to search for planets around cool M-type stars is to use an infrared-sensitive high-dispersion and high-precision spectrograph. Recently, several teams have commissioned NIR spectrographs for high-precision RV surveys, including CARMENES (Calar Alto high-Resolution search for M dwarfs with Exoearths with Near-infrared and optical Echelle Spectrographs; Quirrenbach et al. 2016), HPF (Habitable Planet Finder; Mahadevan et al. 2014), and SPIROU (SPectropolarimetre InfraROUge; Thibault et al. 2012). The RV surveys performed with those spectrographs have so far reported a few detections of planetary systems around M dwarfs cooler than ~ 3000 K (e.g., Zechmeister et al. 2019), while they have reported dozens of exoplanets around stars with effective temperature higher than ~ 3000 K. It is notable that optical RV measurements have been primarily used for those detections; for example, the terrestrial planets around Teegarden’s star were discovered using the optical channel of CARMENES (Zechmeister et al. 2019). High-precision RV measurements in the NIR facilitate the detection of planets around cooler M dwarfs, which remains a frontier in exoplanet exploration.

IRD (InfraRed Doppler instrument) is a high-precision, high-dispersion ($R = 70,000$) NIR spectrograph mounted on the Subaru 8.2-m telescope (Tamura et al. 2012; Kotani et al. 2018). To achieve a velocity precision of $2\text{--}3\text{ ms}^{-1}$, IRD is aided by a wide-band laser-frequency comb (LFC; Kashiwagi et al. 2016; Kokubo et al. 2016), and an adaptive optics, enabling the use of a narrow slit-width. The combination of a large-aperture telescope with high RV precision in the NIR thus makes IRD one of the best instruments for studying cool stars, in particular late M dwarfs, whose flux peaks are located in the NIR. In February 2019, we started an extensive RV survey program for nearby mid-to-late M-type dwarfs within the Subaru Strategic Program (SSP; Sato et al. 2018) framework. This program employs IRD with the aim of detecting planets down to Earth-mass in the habitable zones (HZs) of nearby late M dwarfs. The capabilities of IRD allow the systematic survey of fainter, and thus later-type, M dwarfs than ever before.

In this paper, we present the first exoplanet discovery from the IRD-SSP campaign, a super Earth that orbits near the inner edge of the HZ around Ross 508 (the star is also known as LSPM J1523+1727), which is an M4.5-type dwarf (Koizumi et al. 2021) at a distance of 11.2 pc (Gaia Collaboration et al. 2021) from Earth. In Section 2, we

describe the observations and data reduction of Ross 508. In Section 3 we present our analysis of the fundamental properties and activity of Ross 508, along with the determination of the planet’s orbit from the RV measurements. Finally, in Section 4, we discuss the uniqueness of the planet and its potential formation processes, concluding with a summary.

2 Observations

2.1 Target Selection

Ross 508 was observed as part of the IRD-SSP survey because of its low mass ($M < 0.25 M_{\odot}$), low temperature ($T_{\text{eff}} < 3400$ K), low $v \sin i$ ($< 5\text{ km s}^{-1}$), and low stellar activity. The initial target list was prepared based on literature measurements satisfying the above criteria (Sato et al. 2018) supplemented with optical medium-resolution spectroscopic observations (Koizumi et al. 2021). Stars with no rotation period and $v \sin i$ measurements were required to have nondetections of H α emission, which is expected for inactive and slowly-rotating stars. We continually refine our target list, dropping stars from our long-term monitoring campaign if IRD spectra show them to be double-lined spectroscopic binaries or rapid rotators, or if we detect large RV variations suggestive of stellar companions. With these screening data, we plan to select about 60 mid and late M dwarfs with low RV variability and high RV precision for the RV monitors, after about three-year observations of its planned five-year survey period.

2.2 Observations and Data Reduction

We obtained 102 high-resolution, high S/N spectra of Ross 508 using IRD over ≈ 3 years from 2019 to 2021. All stellar spectra were obtained simultaneously with LFC spectra to provide a fiducial wavelength reference for precision RV measurements. The typical exposure time for each frame was 600 seconds, achieving an S/N ratio of about 90 per pixel at $1\text{ }\mu\text{m}$ wavelength.

The 2 H2RG (HAWAII-2RG) detectors installed in IRD show mutually independent bias levels for each readout channel. We thus used our bias subtraction code optimized for those two detectors to suppress bias counts (Kuzuhara et al. 2018). We also subtracted correlated read noise by applying a commonly used technique for H2RG detectors (e.g., Brandt et al. 2013) to the science pixels in our images with the temporal masks to the 2D-spectra.

Following the removal of bias and read noise, we used IRAF (echelle package) for subsequent échelle data reduction procedures, such as scattered light subtraction, flat fielding, and extraction of one-dimensional spectra.

discovered to host planets via the RV (transit) technique, according to a query of the NASA Exoplanet Archive in February 2022. Note that the effective temperatures from the TESS Input Catalog (TIC; Stassun et al. 2019) were adopted for the majority of the sample.

Table 1. Stellar parameters of Ross 508

Parameter	Value	References
α (J2000.0)	15 ^h 23 ^m 50 ^s .699	<i>Gaia</i> eDR3
δ (J2000.0)	+17°27′37″.30	<i>Gaia</i> eDR3
ϖ (mas)	89.1284 ± 0.0331	<i>Gaia</i> eDR3
Distance (pc)	11.2183 ± 0.0035	Bailer-Jones et al. (2021)
RUWE	1.487	<i>Gaia</i> eDR3
G (mag)	12.1952 ± 0.0029	<i>Gaia</i> eDR3
G_{BP} (mag)	13.9882 ± 0.0044	<i>Gaia</i> eDR3
G_{RP} (mag)	10.9204 ± 0.0042	<i>Gaia</i> eDR3
J (mag)	9.105 ± 0.024	2MASS
K_s (mag)	8.279 ± 0.023	2MASS
Spectral Type	M4.5	Koizumi et al. (2021)
T_{eff} (K)	3071 ⁺³⁴ ₋₂₂	This work
$\log g$ (cgs)	5.039 ± 0.027	This work
L_* (L_{\odot})	3.589 ^{+0.067} _{-0.071} × 10 ⁻³	This work
M_* (M_{\odot})	0.1774 ± 0.0045	This work
R_* (R_{\odot})	0.2113 ± 0.0063	This work
ρ_* (g cm ⁻³)	26.5 ^{+2.5} _{-2.3}	This work
[Fe/H] (dex)	-0.20 ± 0.20	Ishikawa et al. (2022)

Preliminary wavelength calibrations were done using Th-Ar spectra, but we obtained precise RV measurements using LFC spectra (see Hirano et al. 2020, for details). Details of the RV measurements from the 1D spectra are described in Section 3.3.1.

3 Analysis and Results

3.1 Stellar Parameters

We derive the fundamental stellar parameters for Ross 508 using a combination of literature measurements and IRD spectra. Table 1 summarizes all of our adopted stellar parameters including the ones we derive below.

For Ross 508’s metallicity, we adopt its iron abundance [Fe/H] determined by Ishikawa et al. (2022) from the same IRD spectra that we use here. They conducted the equivalent width analysis on the atomic absorption lines of Na, Mg, Ca, Ti, Cr, Mn, Fe, and Sr to derive individual elemental abundances that are consistent with each other. The abundance of individual elements will help to constrain the detailed geophysical properties of the planets, although it is beyond the scope of this paper. Ross 508 is a relatively metal-poor star, but its abundance ratio of each element is consistent with the solar composition within the errors. Their abundance and kinematic analyses show characteristics between the Galactic thin and thick disks, suggesting the possibility of a relatively old population.

We next analyzed the spectral energy distribution (SED) of Ross 508 to estimate its effective temperature and luminosity. The SED was calculated from the mag-

nitudes in the G , B_P , and R_P bands from *Gaia* EDR3 (*Gaia* Collaboration et al. 2021), J , H , and K_s bands from 2MASS (Skrutskie et al. 2006), and $W1$, $W2$, $W3$, and $W4$ bands from WISE (Cutri et al. 2021). We fit BT-Settl synthetic spectrum models (Allard 2014) to the SED using the following parameters: effective temperature T_{eff} , \log surface gravity $\log g$, and $\log(R_s/D)$, where R_s and D are the radius and distance of the star, respectively. We assumed no interstellar extinction. We calculated the posterior probability distributions of these parameters using the Markov Chain Monte Carlo (MCMC) method implemented in the Python package `emcee` (Foreman-Mackey et al. 2013). In each MCMC step, a synthetic spectrum was calculated by linearly interpolating the model grid for a given set of parameters, where the metallicity value was randomly chosen from a normal distribution of $\mathcal{N}(-0.20, 0.20)$ dex. A white noise jitter term, σ_{jitter} , was also fitted for each of the *Gaia* EDR3, 2MASS and WISE data sets such that the magnitude uncertainty was given by $\sqrt{\sigma_{\text{cat}}^2 + \sigma_{\text{jitter}}^2}$, where σ_{cat} is the catalogued uncertainty in magnitude. From the posteriors, we derived $T_{\text{eff}} = 3071^{+34}_{-22}$ K, $\log g = 5.26^{+0.18}_{-0.35}$ (cgs), and $\log(R_s/D) = -9.3721^{+0.0062}_{-0.0085}$ (cgs). Adopting $D = 11.2183 \pm 0.0035$ pc from Bailer-Jones et al. (2021) which is estimated based on the *Gaia*EDR3 parallax, we obtained $R_s = 0.2111^{+0.0030}_{-0.0041} R_{\odot}$, which also yielded the stellar luminosity of $L_s = 3.584^{+0.067}_{-0.071} \times 10^{-3} L_{\odot}$ via the Stefan-Boltzmann law. Note that the median values of the white noise jitter terms are 0.089, 0.074, and 0.00050 mag for the *Gaia* EDR3, 2MASS, and WISE data sets, respectively. The relatively large jitter values in the *Gaia* EDR3 and 2MASS data sets might reflect the challenges for the stellar models for cool stars.

Based on the stellar metallicity reported in Ishikawa et al. (2022), the effective temperature derived above, and the parameters in the literature (i.e., the *Gaia* parallax and 2MASS magnitudes), we inferred the physical parameters of Ross 508, including the stellar mass, which is required to estimate the planet mass. We made use of the empirical formulae by Mann et al. (2015) and Mann et al. (2019) for the stellar radius and mass, for which the apparent K_s -band magnitude of $m_{K_s} = 8.279 \pm 0.023$ mag was adopted from the 2MASS catalog. We implemented a Monte Carlo simulation to estimate the uncertainties of the output parameters, accounting for the statistical error of the input parameters as well as the systematic error of the empirical formulae. We obtained a stellar radius and mass of $0.2113 \pm 0.0063 R_{\odot}$ and $0.1774 \pm 0.0045 M_{\odot}$, respectively, which yield a mean stellar density of $26.5^{+2.5}_{-2.2}$ g cm⁻³ and a surface gravity of $\log g = 5.038 \pm 0.027$ (cgs). This surface gravity is consistent with that derived from

BT-Settl model atmospheres.

3.2 Adaptive optics imaging

Ross 508 has a relatively high renormalized unit weight error (RUWE) of 1.48 in Gaia EDR3, implying that this star might be associated with an unseen companion. In order to search for a possible companion, we analyzed adaptive optics high-resolution images of Ross 508 obtained with the Fiber Injection Monitor (FIM) camera of IRD. FIM is an AO-assisted CCD camera sensitive to wavelengths of 0.83 to 1.05 μm , and is used to monitor a target's position during observations. The CCD camera is usually used to feed the light into the IRD fiber. The FIM observations were performed every time just before RV measurements of IRD, but we selected images taken only under good seeing conditions. The final selected images consist of 33 frames with a total integration time of 74 seconds. The FWHM of the final combined Point Spread Function (PSF) is $0''.19$, and the 5σ raw contrast limit is shown in Figure 1. We also processed archival VLT/NACO data for Ross 508 (program ID: 71.C-0388(A), PI: J.-L. Beuzit) obtained with a narrow-band filter at 2.17 μm (NB 2.17 filter, $2.166 \pm 0.023 \mu\text{m}$) using a well-tested general-use pipeline (Currie et al. 2011). A total of 44 frames with an integration time of 2 seconds each were reduced and combined to create the final high-quality image. No speckle subtraction techniques were applied to either the FIM or NACO images. We found no stellar companions at a separation wider than $\sim 0''.1$ from the central star. At separations exterior to $0''.25$ ($r_{\text{proj}} \sim 2.8$ au), the comparison of the contrast limits with the Baraffe et al. (2003) evolutionary models enables us to rule out companions that are more massive than $35 M_{\text{J}}$ or $70 M_{\text{J}}$ for an assumed system age of 1 Gyr or 10 Gyr, respectively.

3.3 Radial Velocity and Orbital Solutions

3.3.1 Radial Velocity Measurements

For each wavelength-calibrated spectrum, we measured precise RVs following the standard RV-analysis pipeline for IRD (Hirano et al. 2020); we refer to that paper for a detailed discussion. In short, the pipeline extracts the instantaneous instrumental profile (IP) of the spectrograph from the simultaneously injected LFC spectrum, and generates an IP-deconvolved, telluric-free template spectrum for the target star using multiple IRD spectra. Using this template, individual spectral segments for each IRD spectrum are fitted by the forward modeling technique, in which telluric absorption features are simultaneously optimized. The resulting relative RV values as well as their

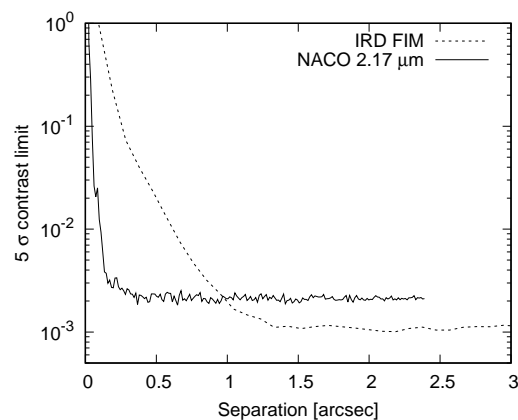


Fig. 1. 5σ contrast limits around Ross 508. The solid line shows the contrast limit from VLT/NACO in the NB 2.17 filter. The dashed line shows the contrast limit from the IRD FIM camera, which has a sensitivity over wavelengths ranging from 0.83 to 1.05 μm

uncertainties are summarized in Table 3. The RV internal error was typically $2\text{--}3 \text{ ms}^{-1}$ for each frame.

We corrected for RV drifts that are attributed to the Earth's rotation and orbital motion (i.e., barycentric RV correction) using the TEMPO2 software (Edwards et al. 2006). TEMPO2 also corrects for perspective acceleration, which is $\approx 0.45 \text{ m s}^{-1} \text{ yr}^{-1}$ for Ross 508. IRD applies multiple readouts to its two H2RG detector during an exposure (Kuzuhara et al. 2018). Accordingly, we computed the telluric RV using the time when half of the total signal was counted, which was determined by monitoring the photon counts acquired by the detectors every ~ 1.5 seconds.

We note that one of the causes of long-term RV measurement instability originates from the IRD instrument. We evaluated the instrumental error via both laboratory experiments and on-sky monitoring observations of an RV standard star, GJ 699. These two methods resulted in the same value of 2 ms^{-1} . From the laboratory experiments, we found that the main sources of instrumental error are the intra- and inter-pixel sensitivity variations of the detector (0.96 ms^{-1}), as well as the modal noise ($\sim 1.2 \text{ ms}^{-1}$) caused by PSF instability (Kotani et al. 2018). We found a total RV error of 3 ms^{-1} over 718 days of on-sky monitoring observations of GJ 699, which (assuming no planet around the star) yields an instrument-derived error of about 2 ms^{-1} (Kotani et al. in prep.). In the case of Ross 508, we assume that the RV measurements are affected by the same amount of instrumental noise. Note that Table 3 provides RV uncertainties that do not include the instrument-derived errors.

3.3.2 Orbital Solutions

We searched for periodicity in our RV time series before performing an orbital fit. We computed the Generalized

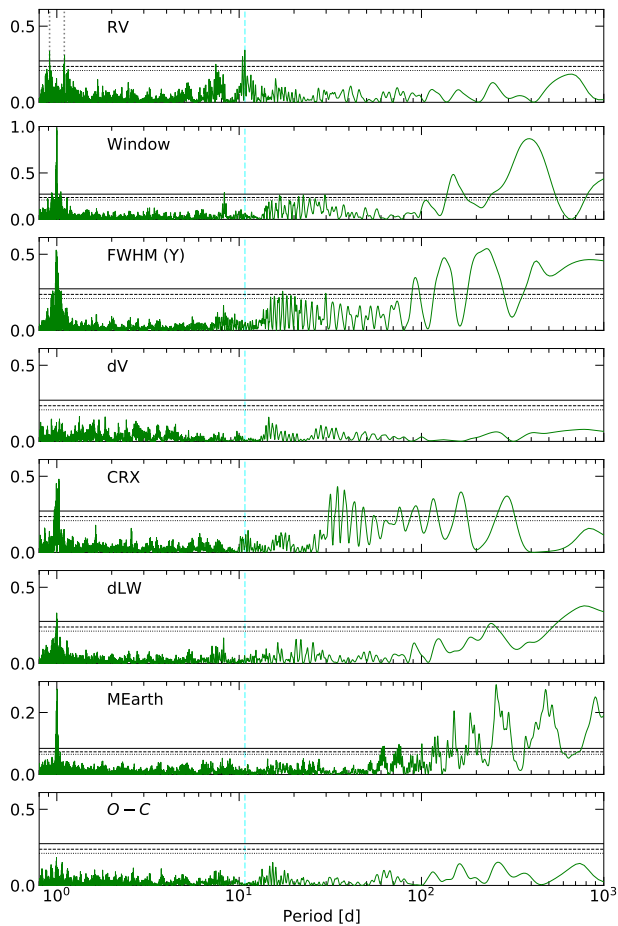


Fig. 2. From top to bottom: GLS periodograms of the RV time series, window function of the RV sampling, FWHM in Y-band region, dV, CRX, dLW, MEarth photometry, and residual of the RV fitting. The dashed cyan vertical line indicates the RV period at 10.7510 days, while the vertical gray lines show the estimated aliases. See the main text for details of those values. The FAP values corresponding to 0.1%, 1%, and 5% are shown with solid, dashed, and dotted lines, respectively.

Lomb-Scargle (GLS) periodogram (Zechmeister & Kürster 2009) for all RV data and for the window function, and identified three significant peaks at 10.7510, 0.9124, and 1.1023 days in order of decreasing GLS power (Figure 2). Hereafter, all the FAP values were derived by analytical estimation reported in Baluev (2008). For the window function, we identified a single peak at 0.9972 days. In the GLS periodogram analysis, we set the RV error to be $\sqrt{\sigma_i^2 + \sigma_{\text{inst}}^2}$, where σ_i is the RV uncertainty of an i -th observation and σ_{inst} is the instrument-derived error described in Section 3.3.1.

Although the RV periodogram shows several significant periodicities, we first investigate whether some of these represent cases of aliasing, which generally appears in periodograms of discretely sampled time series data. To distinguish aliases from physical signals, we performed a simple alias analysis based on the computed periodograms.

In general, when sampling a sine wave of frequency f at sampling frequency f_s , the sample is indistinguishable from any other sample of the sine curve whose frequency is $f_{\text{signal}}(N) = |f - Nf_s|$ (where $N = 0, \pm 1, \pm 2, \dots$, and $f_{\text{signal}}(0) = f$ is the actual signal frequency) as they yield identical sets of data. Those frequencies other than $N = 0$ are aliases that should be addressed. This equation assumes f_s as a perfectly evenly spaced sampling, and of course, the actual observations will not be carried out with such an ideal interval. However, since the window function of our data sampling shows a dominant power on almost a single frequency, we should be able to estimate the approximate effect of aliasing by applying this equation. We here assumed the most significant RV frequency of $1/10.7510 \text{ d}^{-1}$ to be a physical one and the sampling frequency to be the most significant window function peak of $1/0.9972 \text{ d}^{-1}$. If $N = +1$ and $N = -1$, this yields $1/1.0992 \text{ d}^{-1}$ and $1/0.9125 \text{ d}^{-1}$ respectively. These two frequencies are almost identical to those of the second and third significant peaks of the periodogram, showing that those two peaks in the periodogram can be interpreted as alias phenomena associated with a period of 10.751 days and its dominant sampling interval of 0.9972 days. We note that if we assumed the secondary peak of the window function at 390.25 days as a sampling frequency, the aliases were 11.05 and 10.46 days in the case of $N = +1$ and $N = -1$, respectively. The 10.46 days alias is almost identical to a peak of 10.45 days in the periodogram though its frequency is far beyond the Nyquist frequency of $0.5f_s = 1/780.5$.

With a single significant periodicity at 10.75 days, we next performed a Keplerian fit to the RVs. As discussed in Section 3.4, we found no significant activity signals at this period. We used `emcee` to explore the parameter spaces via MCMC. The initial states were randomly generated from the prior distributions shown in Table 2. We ran the sampler until it satisfied the following convergence criterion: if the number of steps is greater than 100 times the autocorrelation length of each parameter, which is estimated every 1000 steps, and this estimate varies by less than 1%, then we assume that the chain has converged. The maximum steps was set to 30 millions. The first 20% of the steps were discarded as burn-in, yielding a total of 24.0M samples of the posterior distribution from the remaining steps.

Based on Gregory (2005), the likelihood function \mathcal{L} used in this analysis is

$$\ln \mathcal{L} = -\frac{1}{2} \sum_i \left(\frac{(v_{i,\text{obs}} - v_{i,\text{model}})^2}{\sigma_i^2 + \sigma_{\text{jitt}}^2} + \ln(\sigma_i^2 + \sigma_{\text{jitt}}^2) \right), \quad (1)$$

where $v_{i,\text{obs}}$ is the i -th observed RV, $v_{i,\text{model}}$ is i -th RV

model calculated from the companion’s Keplerian orbital motion, and σ_{jitt} is a jitter parameter to account for RV variations due to stellar activity and changes in instrumental stability. Priors of the parameters, best-fit orbital solutions and their uncertainties are presented in Table 2, where K_b is the velocity semi-amplitude, P is the orbital period, T_p is the time of periastron passage, e is the eccentricity, ω is the argument of periastron, γ is the constant velocity, and $\dot{\gamma}$ is the constant RV acceleration (i.e. linear RV trend). The M_b , i and a_b denote the mass of the planet, orbital inclination relative to line-of-sight and its orbital semimajor axis, respectively.

A relatively large offset in RV measurements appears on August and September of 2021 (See Fig. 8). We wondered if these observations were influenced by a possible irregular and temporal offset in our RV measurements possibly caused by an instability of the instrument or a high activity event such as flaring. Indeed, although the LFC’s spectra have been stabilized for several years, the observing runs at August and September 2021 were immediately after the restoration from the irregular operation of the temperature stabilization room in which the LFC instrument are placed. Therefore, we compared two RV models: A) one does not consider the RV offset in this period, B) another assumes the RV offset as an additional systemic RV offset parameter in the RV model (γ_2).

We report the posterior median and 1σ credible region for each parameter in Table 2. In our analysis, we compared four RV models in total:

- A1) Single planet,
- A2) Model A1 + linear RV trend,
- B1) Single planet with RV offset for data in August and September of 2021 (i.e. γ_2), and
- B2) Model B1 + linear RV trend.

To perform model selection, we calculated the Akaike Information Criterion (AIC; Akaike 1974) and Bayesian Information Criterion (BIC; Schwarz 1978) for each of the four models, which are defined as

$$\text{AIC} = 2k - 2\ln \mathcal{L} \quad (2)$$

and

$$\text{BIC} = k \ln(N) - 2\ln \mathcal{L}, \quad (3)$$

respectively, where k is the number of parameters, N is the number of data points, and \mathcal{L} is the maximum likelihood of the model.

Figure 3 shows the observed RVs and the orbital solutions from our MCMC analysis, and Figure 4 shows a “corner” plot of the covariance between the parameters in our MCMC analysis. The BIC value is smaller for the model A1 than that of the model A2 while the AIC value

is not. The ΔAIC and ΔBIC are only slightly different from the values at which a model selection is statistically meaningful (Kass & Raftery 1995). We also found no clear statistical difference in the comparison between the B1 and B2, as indicated by the comparable BIC values. While Model A2 suggests a long-term trend, Model B2 did not, suggesting a degeneracy between the models of the linear RV trend and the temporal RV offset. Further investigation and additional data can resolve the degeneracy, but we here conclude that there is no clear evidence to identify a long-term linear trend in our RV measurements.

The posterior eccentricity distribution of the model A1 monotonically decreases with a maximum at zero (Figure 9 in the Appendix); we report only the 3σ upper limit for the eccentricity. Meanwhile, the posterior distributions of eccentricity for models A2, B1, and B2 have a maximum likelihood value around 0.3. However, a zero eccentricity is still likely as indicated by the eccentricity posterior in these three models. We therefore conclude that only an extremely high-eccentricity, $e > 0.9$ (3σ), is unlikely. Furthermore, we adopt the model B1 (i.e., inclusion of no linear RV trend and a systematic RV offset) as our fiducial model based on the lowest AIC/BIC value among the four models.

3.4 Stellar Activity

3.4.1 Photometric Variability

While the RV data are well-fit by a planetary companion, we now assess whether stellar activity could instead be responsible. To search for photometric modulation caused by stellar surface magnetic activity, we used the public archive data from the MEarth-North project (Berta et al. 2012) and the “All-Sky Automated Survey for Supernovae” (ASAS-SN; Shappee et al. 2014). We analyzed the MEarth data for Ross 508 from Data Release 10, and we selected data observed with the same telescope and RG715 filter bandpass at MEarth-North. We analyzed the g-band data from ASAS-SN. TESS will observe this target in Sector 51 (April to May 2022), which will allow us to characterize the stellar activity in more detail.

Newton et al. (2016) were not able to detect the rotation period of Ross 508. We independently analyzed the photometric data both from the MEarth and the ASAS-SN, and found no clear signals in the GLS periodogram that could be due to rotation or that match the observed RV signal (Figure 2 for the periodogram on the MEarth light curves). In order to evaluate how small of a stellar-rotation modulation MEarth data can detect, we estimated the sensitivity of the MEarth data set to photometric modulation by creating 100 sinusoidal curves with periods of 10.8 days (same

Table 2. RV posterior distributions and priors. *

Parameter	Model A1	Model A2	Model B1	Model B2	Prior	Bound
K_b (ms ⁻¹)	3.80 ^{+0.62} _{-0.58}	3.90 ^{+0.67} _{-0.61}	3.92 ^{+0.60} _{-0.58}	3.95 ^{+0.63} _{-0.59}	Uniform	(0, 10)
P (d)	10.76 ^{+0.01} _{-0.02}	10.77 ^{+0.01} _{-0.01}	10.77 ^{+0.01} _{-0.01}	10.77 ^{+0.01} _{-0.01}	Uniform	(9, 12)
T_p (BJD -2450000)	9370.22 ^{+1.38} _{-1.88}	9370.63 ^{+0.80} _{-0.84}	9370.24 ^{+0.64} _{-0.71}	9370.34 ^{+0.65} _{-0.60}	Uniform	2459370 + (-6, +6)
e	0 (< 0.70; 3 σ)	0.33 ^{+0.15} _{-0.17}	0.33 ^{+0.13} _{-0.15}	0.36 ^{+0.14} _{-0.16}	Uniform	(0, 0.99)
ω (rad)		-0.41 ^{+0.49} _{-0.50}	-0.65 ^{+0.39} _{-0.48}	-0.63 ^{+0.38} _{-0.44}	Uniform	($-\pi$, $+\pi$)
σ_{jitt} (ms ⁻¹)	2.52 ^{+0.43} _{-0.41}	2.26 ^{+0.44} _{-0.42}	1.76 ^{+0.46} _{-0.48}	1.73 ^{+0.48} _{-0.49}	Uniform	(0, 20)
γ (ms ⁻¹)	-0.65 ^{+0.38} _{-0.38}	-0.28 ^{+0.38} _{-0.38}	-0.19 ^{+0.34} _{-0.34}	-0.08 ^{+0.35} _{-0.35}	Uniform	(-20, +20)
γ_2 (ms ⁻¹)			-7.68 ^{+1.26} _{-1.31}	-6.61 ^{+1.44} _{-1.36}	Uniform	(-20, +20)
$\dot{\gamma}$ (ms ⁻¹ yr ⁻¹)		2.03 ^{+0.62} _{-0.62}		0.89 ^{+0.62} _{-0.60}	Uniform	(-10, +10)
$M_b \sin i$ (M_{\oplus})	3.99 ^{+0.60} _{-0.60}	3.96 ^{+0.59} _{-0.59}	4.00 ^{+0.53} _{-0.55}	3.97 ^{+0.54} _{-0.58}		
a_b (au)	0.05353 ^{+0.00047} _{-0.00051}	0.05361 ^{+0.00047} _{-0.00048}	0.05366 ^{+0.00056} _{-0.00049}	0.05356 ^{+0.00048} _{-0.00056}		
rms (ms ⁻¹)		3.73	3.29	3.27		
# of Samples	16.0 M	13.8 M	24.0 M	20.5 M		
AIC	582.63**	573.79	553.63	553.44		
BIC	600.94**	602.56	582.39	584.82		
Description	Single planet	Model A1 + Linear Trend	Single planet + γ_2	Model B1 + Linear Trend		

* The e and ω were derived from $\sqrt{e} \sin(\omega)$ and $\sqrt{e} \cos(\omega)$.

**

Assumed $e = 0$ as the best-fit value.

as the detected planet’s orbital period), with the same cadence as the actual MEarth data. We added white noise to each data point by sampling a Gaussian distribution with standard deviation equal to the individual photometric uncertainty of the corresponding data point, after scaling the median of the uncertainties to the standard deviation of all the data points in the MEarth light curve. We then applied a periodogram analysis to these mock data. We repeated the above analysis varying the amplitudes of the sinusoidal curves. As per our definition, a periodic signal at 10.8 days can be detected if the False Alarm Probability (FAP) at that period is less than 1%. We found that 70% of the simulations yield a detection of the 10.8-day sinusoidal signal if its amplitude is larger than 0.4% of the stellar brightness in the MEarth photometric band. Similar results were obtained even if we shifted the phase of the sinusoidal signal or directly injected the sinusoidal curves into the MEarth light curves instead of creating mock data. However, even if there were a cool spot that produces a light-curve variation equal to or smaller than 0.4%, the corresponding RV semi-amplitude would be too small to account for our detected RV amplitude. Assuming the star’s effective temperature, spot temperature, and rotation velocity ($v \sin i$) to be 3000 K, 2500 K, and 1 km s⁻¹, respectively, such a cool spot would induce an RV semi-amplitude of no more than 2 m s⁻¹. Here, the $v \sin i$ of 1 km s⁻¹ is the maximum value estimated from the stellar radius of 0.213 R_{\odot} (see Table 1), assuming a rotation period equal to the detected RV period. Thus, a cool spot rotating with a period of 10.8 days and covering an area smaller than 0.4% of the stellar

surface cannot reproduce our identified RV variation. Our light-curve analysis suggests that the 10.75 days signal is not caused by a cool spot on the stellar surface. We note that this analysis only applies if the phase of the photometric modulation is coherent over the ≈ 3 year baseline of the IRD observations. However, the same criterion applies to the RV signal itself, which is indeed coherent in phase over this baseline.

3.4.2 Line Profile Variation

We next determine whether there is periodicity in the line profile at a period matching that of our recovered planet. We apply the least-squares deconvolution (LSD) method (Kochukhov et al. 2010) to derive mean line profiles. A list of lines is empirically built from an IP-deconvolved, telluric-free template spectrum. To minimize contamination, we use spectra within 1000–1070 nm, which contain fewer telluric lines. The uncertainties of the LSD profiles are determined with formal uncertainties scaled by the standard deviations of the difference between each individual LSD and the mean profile. As indicators of line profile variation, we computed the full width at half maximum (FWHM; the line width) and BiGauss (dV; the line asymmetry) by fitting Gaussian functions (Santerne et al. 2015). We also computed the chromatic index (CRX; the wavelength dependence of RV) and the differential line width (dLW; the line width) (Zechmeister et al. 2018). To compute the dLW, we used a template spectrum convolved with the averaged IP instead of a coadded spectrum to avoid telluric-line contamination. To determine the CRX,

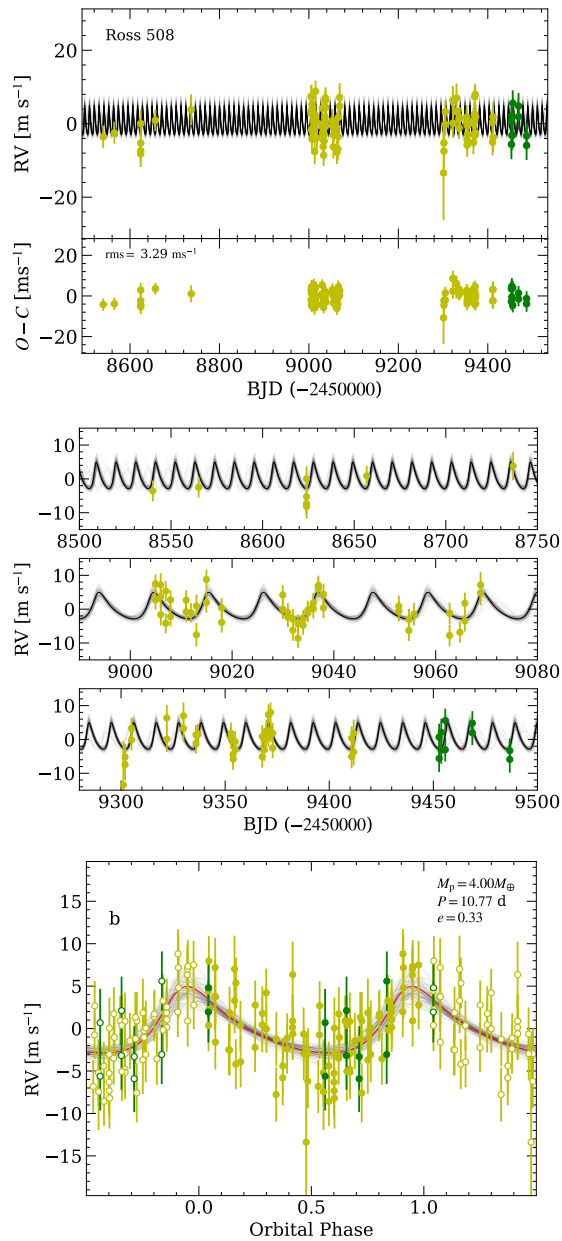


Fig. 3. Observed RVs and the best-fit orbital solution based on the MCMC method of Model B1 (red line). Yellow circles with error bars represent the observed RVs and their uncertainties, respectively. Green circles and error bars show the same as yellow ones, but obtained in August and September 2021. Gray lines represent 100 RV model curves randomly selected from the posterior. The error bars are the quadrature sum of the measurement uncertainties with the best-fit value of the jitter parameter σ_{jitter} . *Top:* the best-fit RV curve (top) and the residuals of the fit (bottom). *Middle:* Zoom up of each data segment. *Bottom:* Phase-folded RV variations. Red line represents the best-fit RV model.

the wavelength range is binned from 1000 nm to 1750 nm in 10 nm increments, and we use the weighted average of the RVs of the segments in each bin.

The GLS periodograms of all stellar activity indicators are shown in Figure 2. None of the activity indicators exhibit any significant peaks at 10.75 days. Figure 5 shows the evolution of GLS power at 10.75 d for the RVs and activity indicators. While the power increases with the number of data points for the RVs, the power remains consistently low for the activity indicators, suggesting that the periodic RV variations are not induced by stellar activity (e.g. Mortier & Collier Cameron 2017).

4 Summary and Discussion

In the previous section, we showed that the M4.5 dwarf Ross 508 has a significant RV periodicity at 10.75 days with possible aliases at 1.099 and 0.913 days. This periodicity has no counterpart in photometry or stellar activity indicators, but is well-fit by a Keplerian orbit due to a new planet, Ross 508 b. Our newly discovered planet, Ross 508 b, has a minimum mass of $4.0 M_{\oplus}$ and a semi-major axis of 0.05 au.

We explored four possible scenarios to explain the measured RV data. We examined models including a presence of RV offset to the data obtained in August and September 2021, and a long-term RV trend, which might be caused by an unseen companion, because Ross 508 has a relatively high renormalized unit weight error (RUWE) of 1.48 in Gaia EDR3, suggesting that it is poorly fit by a single star model. Of 19 comparison stars in EDR3 with parallaxes between 80 and 100 mas and $B_P - R_P$ colors within 0.3 mag of that of Ross 508, just three have RUWE values higher than 1.48.

While the differences between the four models are not large, we found that a $\sim 7 \text{ ms}^{-1}$ RV offset and the absence of a long-term RV trend best explain the observed data. In this scenario, the peak of the posterior distribution of the eccentricity is around 0.3, but the distribution is wide all the way down to zero; hence it does not constrain the eccentricity well. As a reference, some previously known exoplanets around late-M dwarfs have eccentricities reported as upper limits, such as GJ 1061 b ($e < 0.31$), GJ 1061 d ($e < 0.53$; Dreizler et al. 2020) and Proxima Centauri b ($e < 0.35$; Anglada-Escudé et al. 2016; Brown 2017). Further RV measurements of Ross 508 will clarify whether the planet has a high eccentricity among the sample of known super-Earths around mid-to-late M stars ($T_{\text{eff}} < 3200 \text{ K}$, $M_p \sin i < 10 M_{\oplus}$), providing important clues about their origin.

As well as other super Earths with orbital periods much

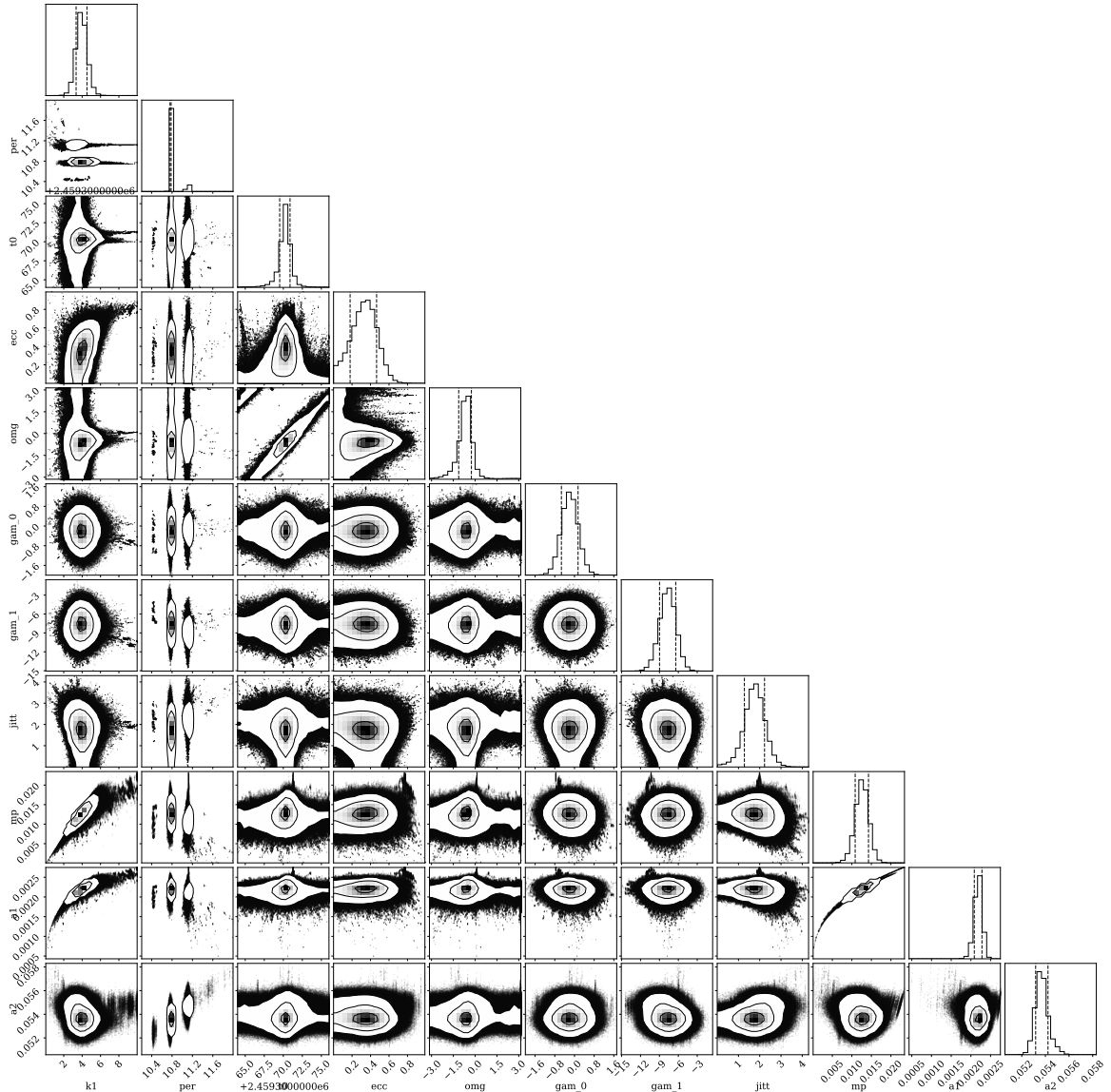


Fig. 4. Corner plot of the posterior distributions of Model B1.

shorter than the snow line around their host stars, Ross 508 b may have formed beyond the snow line (~ 0.16 au) and undergone inward Type I migration (Goldreich & Tremaine 1979; Ogiwara & Ida 2009; Izidoro et al. 2017). Even if the eccentricity of a migrating planet is initially high, it can be damped by the force exerted on the planet by density waves (e.g., Tanaka & Ward 2004). Thus, the solution of a single-planet system with zero or low eccentricity is compatible with the Type I migration scenario. Alternatively, there remains the possibility that Ross 508 b is in a high eccentricity orbit. In a multiple-planet system, migrated planets experience giant impacts or are trapped in a resonant chain (e.g., Ogiwara & Ida 2009; Izidoro et al. 2017). Planetary eccentricities are excited by giant im-

pacts. The eccentricity of a planet can be also excited by gravitational interactions between neighboring planets or secular perturbations from a (sub)stellar companion on a wider orbit. The confirmation of a long-term RV trend will help disentangle the formation history of the super-Earth Ross 508 b.

The habitability of a planet primarily depends on the time-averaged stellar flux $\langle F \rangle$ that it receives over an entire orbit (Williams & Pollard 2002): $\langle F \rangle = F/\sqrt{1-e^2}$, where F is the stellar flux at the semimajor axis of a planet and e is the eccentricity of a planet. As shown in Figure 6, the average insolation of Ross 508 b with an eccentricity ranging from 0 to 0.9 (which corresponds to 3σ limit) is always higher than the runaway greenhouse limit for

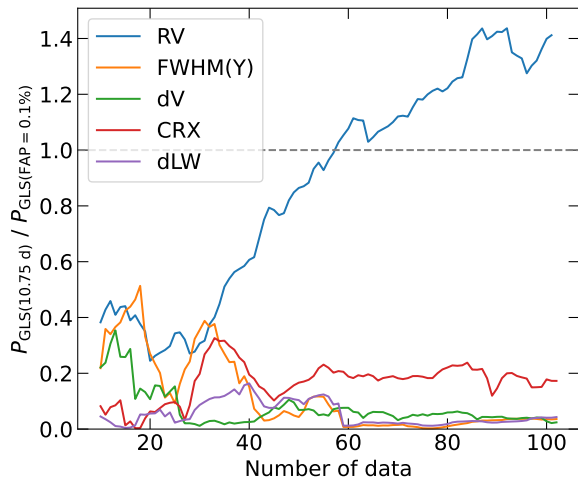


Fig. 5. Significance of the periodogram power for RVs and for all line-profile indexes as the number of data points increases. Significances are measured as fractions of the GLS power corresponding to $FAP = 0.1\%$; the dashed gray horizontal line shows a value corresponding to $FAP = 0.1\%$ (i.e. 1.0). The powers for RVs, FWHM(Y), dV, CRX, and dLW are respectively shown in blue, orange, green, red, and purple.

an Earth-sized aquaplanet around M dwarfs (Kopparapu et al. 2017). We note that the runaway greenhouse limit shown in Figure 6 was estimated for an Earth-sized planet around a low-mass star with $[Fe/H]=0$. The inner edge of the habitable zone may be farther from Ross 508 than what we calculated above because the low metallicity ($[Fe/H] = -0.2$) of Ross 508 yields a lower stellar luminosity (Kopparapu et al. 2016). Also, the habitability of super-Earths can be affected by climate and mantle dynamics, such as plate tectonics (e.g., Miyagoshi et al. 2018). The detailed characterization of Ross 508 helps understand the habitability of a super-Earth.

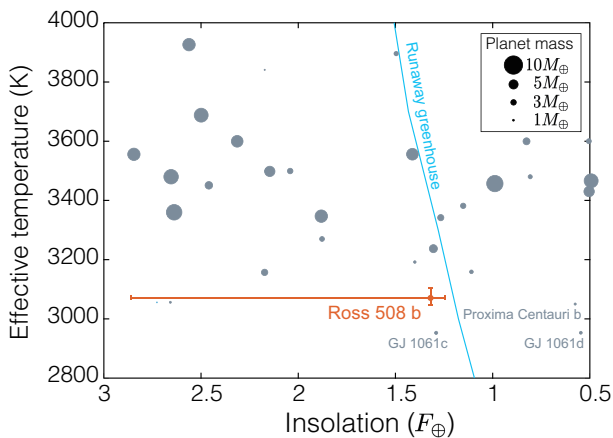


Fig. 6. Planets with masses below $10 M_{\oplus}$ around stars with $2800 K \leq T_{\text{eff}} \leq 4000 K$. Ross 508 b is located near the runaway greenhouse limit as the inner edge of a habitable zone for an Earth-sized aquaplanet around M dwarfs (Kopparapu et al. 2017). The error bar of Ross 508's insolation is based on the 3σ limit on its eccentricity.

For compositional and atmospheric characterizations, it is advantageous if Ross 508 b transits the host star. The geometric transit probability (e.g., Kane & von Braun 2009) of Ross 508 b based on the best-fit orbital parameters (Model B1) is estimated to be $\approx 1.6\%$, a small probability but it is worth searching for their signals given the brightness of Ross 508 especially in the near infrared. We visually inspected Ross 508's light curves by MEarth (Section 3.4), and found no evidence for planetary transits of Ross 508 b. Fortunately, TESS is scheduled to observe Ross 508 in Sector 51 (April to May 2022), which would deliver Ross 508's light curve with a better precision. Provided that Ross 508 b has an internal composition similar to Earth, the expected depth of the transit is $\approx 0.3\%$, which is easily identified by the TESS photometry. Future atmospheric characterization of Ross 508 b makes it possible to explore the bulk composition of Ross 508 b and the formation mechanism of a massive terrestrial planet orbiting near the habitable zone.

Figure 7 places Ross 508 b in context with planetary systems around other nearby M-dwarfs; Ross 508 is one of the faintest, lowest-mass stars with an RV-detected planet. RV monitoring of such a faint, red star requires both a large telescope aperture and a high-precision spectrograph in the near-infrared. Future surveys with IRD and other high-precision NIR spectrographs will enable the discovery of planets around more stars like Ross 508, and will establish the diversity of their planetary systems. Exoplanet exploration will be advanced by the other late-M dwarf RV surveys using high-dispersion spectrographs, such as HPF, CARMENES, and SPIROU, as well as exoplanet surveys using the transit technique from space (e.g., TESS) and the ground (e.g., SPECULOOS; Delrez et al. 2018). Hence, the findings from various late-M dwarf observing campaigns in the 2020s will be combined to provide important clues to reveal the true nature of planetary systems around cool M dwarfs.

Acknowledgments

This research is based on data collected at the Subaru Telescope, which is operated by the National Astronomical Observatory of Japan. We are honored and grateful for the opportunity of observing the Universe from Maunakea, which has the cultural, historical, and natural significance in Hawaii. M.T. is supported by JSPS KAKENHI grant Nos. 18H05442, 15H02063, and 22000005. YH was partly supported by a Grant-in-Aid for Scientific Research on Innovative Areas (JSPS KAKENHI Grant Number 18H05439). This work is partly supported by JSPS KAKENHI Grant Numbers JP18H05439 and JP21K20388, JST CREST Grant Number JPMJCR1761, the Astrobiology Center of National Institutes of Natural Sciences (NINS) (Grant Number AB031010). This research

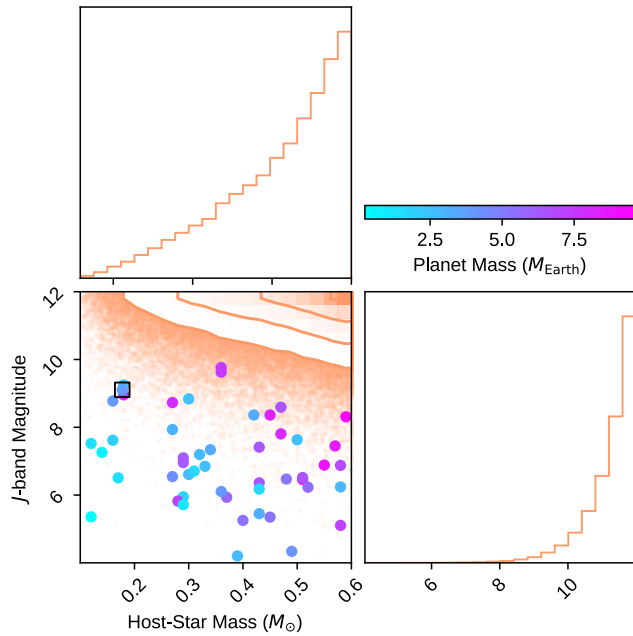


Fig. 7. Masses (M_{\odot}) and J -band magnitudes (mag) of M -type dwarfs that host RV-discovered planetary systems. The background contour shows the nearby M -type dwarfs taken from the TIC catalogue (Stassun et al. 2019). The filled circles are from the NASA exoplanet archive, with their J -band magnitudes from the 2MASS catalogue (Skrutskie et al. 2006). Note that we here plot only planetary-systems hosting planets with masses lower than $10 M_{\text{Earth}}$. Ross 508, with parameters taken from Table 1, is enclosed by a square box. The masses of the lowest-mass planets (which are also from the NASA Exoplanet Archive) in the systems are indicated by the color bar at the right side of the upper panel. A low-mass planet recently discovered around Proxima Centauri (Faria et al. 2022) was included in the plots.

has made use of the SIMBAD database, operated at CDS, Strasbourg, France (Wenger et al. 2000). This research made use of Astropy,² a community-developed core Python package for Astronomy (Astropy Collaboration et al. 2013, 2018). This research has made use of the NASA Exoplanet Archive (<https://exoplanetarchive.ipac.caltech.edu>), which is operated by the California Institute of Technology, under contract with the National Aeronautics and Space Administration under the Exoplanet Exploration Program. This research has made use of data obtained from or tools provided by the portal exoplanet.eu of The Extrasolar Planets Encyclopaedia. The `corner` (Foreman-Mackey 2016) Python module has been helpful to create the figures in this paper.

References

- Akaike, H. 1974, *IEEE Transactions on Automatic Control*, 19, 716, doi: 10.1109/TAC.1974.1100705
- Allard, F. 2014, in *Exploring the Formation and Evolution of Planetary Systems*, ed. M. Booth, B. C. Matthews, & J. R. Graham, Vol. 299, 271–272, doi: 10.1017/S1743921313008545
- Anglada-Escudé, G., Amado, P. J., Barnes, J., et al. 2016, *Nature*, 536, 437, doi: 10.1038/nature19106
- Astropy Collaboration, Robitaille, T. P., Tollerud, E. J., et al. 2013, *A&A*, 558, A33, doi: 10.1051/0004-6361/201322068
- Astropy Collaboration, Price-Whelan, A. M., Sipőcz, B. M., et al. 2018, *AJ*, 156, 123, doi: 10.3847/1538-3881/aabc4f
- Baglin, A., Auvergne, M., Barge, P., et al. 2006, in *ESA Special Publication, Vol. 1306, The CoRoT Mission Pre-Launch Status - Stellar Seismology and Planet Finding*, ed. M. Fridlund, A. Baglin, J. Lochard, & L. Conroy, 33
- Bailer-Jones, C. A. L., Rybizki, J., Fouesneau, M., Demleitner, M., & Andrae, R. 2021, *AJ*, 161, 147, doi: 10.3847/1538-3881/abd806
- Baluev, R. V. 2008, *MNRAS*, 385, 1279, doi: 10.1111/j.1365-2966.2008.12689.x
- Baraffe, I., Chabrier, G., Barman, T. S., Allard, F., & Hauschildt, P. H. 2003, *A&A*, 402, 701, doi: 10.1051/0004-6361:20030252
- Berta, Z. K., Irwin, J., Charbonneau, D., Burke, C. J., & Falco, E. E. 2012, *AJ*, 144, 145, doi: 10.1088/0004-6256/144/5/145
- Borucki, W. J., Koch, D., Basri, G., et al. 2010, *Science*, 327, 977, doi: 10.1126/science.1185402
- Brandt, T. D., McElwain, M. W., Turner, E. L., et al. 2013, *ApJ*, 764, 183, doi: 10.1088/0004-637X/764/2/183
- Brown, R. A. 2017, *ApJ*, 844, 100, doi: 10.3847/1538-4357/aa621a
- Currie, T., Burrows, A., Itoh, Y., et al. 2011, *ApJ*, 729, 128, doi: 10.1088/0004-637X/729/2/128
- Cutri, R. M., Wright, E. L., Conrow, T., et al. 2021, *VizieR Online Data Catalog*, II/328
- Delrez, L., Gillon, M., Queloz, D., et al. 2018, in *Society of Photo-Optical Instrumental Engineers (SPIE) Conference Series, Vol. 10700, Ground-based and Airborne Telescopes VII*, ed. H. K. Marshall & J. Spyromilio, 107001I, doi: 10.1117/12.2312475
- Dreizler, S., Jeffers, S. V., Rodríguez, E., et al. 2020, *MNRAS*, 493, 536, doi: 10.1093/mnras/staa248
- Edwards, R. T., Hobbs, G. B., & Manchester, R. N. 2006, *MNRAS*, 372, 1549, doi: 10.1111/j.1365-2966.2006.10870.x
- Faria, J. P., Suárez Mascareño, A., Figueira, P., et al. 2022, *A&A*, 658, A115, doi: 10.1051/0004-6361/202142337
- Foreman-Mackey, D. 2016, *The Journal of Open Source Software*, 1, 24, doi: 10.21105/joss.00024
- Foreman-Mackey, D., Hogg, D. W., Lang, D., & Goodman, J. 2013, *PASP*, 125, 306, doi: 10.1086/670067
- Gaia Collaboration, Brown, A. G. A., Vallenari, A., et al. 2021, *A&A*, 650, C3, doi: 10.1051/0004-6361/202039657e
- Gillon, M., Triaud, A. H. M. J., Demory, B.-O., et al. 2017, *Nature*, 542, 456, doi: 10.1038/nature21360
- Goldreich, P., & Tremaine, S. 1979, *ApJ*, 233, 857, doi: 10.1086/157448
- Gregory, P. C. 2005, *ApJ*, 631, 1198, doi: 10.1086/432594
- Hirano, T., Kuzuhara, M., Kotani, T., et al. 2020, *PASJ*, 72, 93, doi: 10.1093/pasj/psaa085
- Ishikawa, H. T., Aoki, W., Hirano, T., et al. 2022, *AJ*, 163, 72, doi: 10.3847/1538-3881/ac3ee0
- Izidoro, A., Ogihara, M., Raymond, S. N., et al. 2017, *MNRAS*, 470, 1750, doi: 10.1093/mnras/stx1232

² <http://www.astropy.org>

- Kane, S. R., & von Braun, K. 2009, *PASP*, 121, 1096, doi: 10.1086/606062
- Kashiwagi, K., Kurokawa, T., Okuyama, Y., et al. 2016, *Opt. Express*, 24, 8120, doi: 10.1364/OE.24.008120
- Kass, R. E., & Raftery, A. E. 1995, *Journal of the American Statistical Association*, 90, 773, doi: 10.1080/01621459.1995.10476572
- Kochukhov, O., Makaganiuk, V., & Piskunov, N. 2010, *A&A*, 524, A5, doi: 10.1051/0004-6361/201015429
- Koizumi, Y., Kuzuhara, M., Omiya, M., et al. 2021, *PASJ*, 73, 154, doi: 10.1093/pasj/psaa112
- Kokubo, T., Mori, T., Kurokawa, T., et al. 2016, in *Advances in Optical and Mechanical Technologies for Telescopes and Instrumentation II*, ed. R. Navarro & J. H. Burge, Vol. 9912, International Society for Optics and Photonics (SPIE), 599 – 604, doi: 10.1117/12.2232221
- Kopparapu, R. k., Wolf, E. T., Arney, G., et al. 2017, *ApJ*, 845, 5, doi: 10.3847/1538-4357/aa7cf9
- Kopparapu, R. k., Wolf, E. T., Haqq-Misra, J., et al. 2016, *ApJ*, 819, 84, doi: 10.3847/0004-637X/819/1/84
- Kotani, T., Tamura, M., Nishikawa, J., et al. 2018, in *Society of Photo-Optical Instrumentation Engineers (SPIE) Conference Series*, Vol. 10702, Ground-based and Airborne Instrumentation for Astronomy VII, ed. C. J. Evans, L. Simard, & H. Takami, 1070211, doi: 10.1117/12.2311836
- Kuzuhara, M., Hirano, T., Kotani, T., et al. 2018, in *Society of Photo-Optical Instrumentation Engineers (SPIE) Conference Series*, Vol. 10702, Ground-based and Airborne Instrumentation for Astronomy VII, ed. C. J. Evans, L. Simard, & H. Takami, 1070260
- Lissauer, J. J., Fabrycky, D. C., Ford, E. B., et al. 2011, *Nature*, 470, 53, doi: 10.1038/nature09760
- Mahadevan, S., Ramsey, L. W., Terrien, R., et al. 2014, in *Society of Photo-Optical Instrumentation Engineers (SPIE) Conference Series*, Vol. 9147, Ground-based and Airborne Instrumentation for Astronomy V, ed. S. K. Ramsay, I. S. McLean, & H. Takami, 91471G, doi: 10.1117/12.2056417
- Mann, A. W., Feiden, G. A., Gaidos, E., Boyajian, T., & von Braun, K. 2015, *ApJ*, 804, 64, doi: 10.1088/0004-637X/804/1/64
- Mann, A. W., Dupuy, T., Kraus, A. L., et al. 2019, *ApJ*, 871, 63, doi: 10.3847/1538-4357/aaf3bc
- Mayor, M., & Queloz, D. 1995, *Nature*, 378, 355, doi: 10.1038/378355a0
- Miyagoshi, T., Kameyama, M., & Ogawa, M. 2018, *Earth, Planets and Space*, 70, 200, doi: 10.1186/s40623-018-0975-5
- Mortier, A., & Collier Cameron, A. 2017, *A&A*, 601, A110, doi: 10.1051/0004-6361/201630201
- Newton, E. R., Irwin, J., Charbonneau, D., et al. 2016, *ApJ*, 821, 93, doi: 10.3847/0004-637X/821/2/93
- Ogihara, M., & Ida, S. 2009, *ApJ*, 699, 824, doi: 10.1088/0004-637X/699/1/824
- Quirrenbach, A., Amado, P. J., Caballero, J. A., et al. 2016, in *Society of Photo-Optical Instrumentation Engineers (SPIE) Conference Series*, Vol. 9908, Ground-based and Airborne Instrumentation for Astronomy VI, ed. C. J. Evans, L. Simard, & H. Takami, 990812, doi: 10.1117/12.2231880
- Ricker, G. R., Winn, J. N., Vanderspek, R., et al. 2015, *Journal of Astronomical Telescopes, Instruments, and Systems*, 1, 014003, doi: 10.1117/1.JATIS.1.1.014003
- Santerne, A., Díaz, R. F., Almenara, J. M., et al. 2015, *MNRAS*, 451, 2337, doi: 10.1093/mnras/stv1080
- Sato, B., Ohashi, N., Akiyama, E., et al. 2018, Subaru Strategic Program proposal, https://www.naoj.org/Science/SACM/Senryaku/IRD_180520235849.pdf
- Schneider, J., Dedieu, C., Le Sidaner, P., Savalle, R., & Zolotukhin, I. 2011, *A&A*, 532, A79, doi: 10.1051/0004-6361/201116713
- Schwarz, G. 1978, *The Annals of Statistics*, 6, 461, doi: 10.1214/aos/1176344136
- Shappee, B. J., Prieto, J. L., Grupe, D., et al. 2014, *ApJ*, 788, 48, doi: 10.1088/0004-637X/788/1/48
- Skrutskie, M. F., Cutri, R. M., Stiening, R., et al. 2006, *AJ*, 131, 1163, doi: 10.1086/498708
- Stassun, K. G., Oelkers, R. J., Paegert, M., et al. 2019, *The Astronomical Journal*, 158, 138, doi: 10.3847/1538-3881/ab3467
- Tamura, M., Suto, H., Nishikawa, J., et al. 2012, in *Society of Photo-Optical Instrumentation Engineers (SPIE) Conference Series*, Vol. 8446, Ground-based and Airborne Instrumentation for Astronomy IV, ed. I. S. McLean, S. K. Ramsay, & H. Takami, 84461T, doi: 10.1117/12.925885
- Tanaka, H., & Ward, W. R. 2004, *ApJ*, 602, 388, doi: 10.1086/380992
- Teng, H.-Y., Sato, B., Takarada, T., et al. 2022, *PASJ*, 74, 92, doi: 10.1093/pasj/psab112
- Thibault, S., Rabou, P., Donati, J.-F., et al. 2012, in *Society of Photo-Optical Instrumentation Engineers (SPIE) Conference Series*, Vol. 8446, Ground-based and Airborne Instrumentation for Astronomy IV, ed. I. S. McLean, S. K. Ramsay, & H. Takami, 844630, doi: 10.1117/12.926697
- Vanderburg, A., Rappaport, S. A., Xu, S., et al. 2020, *Nature*, 585, 363, doi: 10.1038/s41586-020-2713-y
- Wenger, M., Ochsenbein, F., Egret, D., et al. 2000, *A&AS*, 143, 9, doi: 10.1051/aas:2000332
- Williams, D. M., & Pollard, D. 2002, *International Journal of Astrobiology*, 1, 61, doi: 10.1017/S1473550402001064
- Zechmeister, M., & Kürster, M. 2009, *A&A*, 496, 577, doi: 10.1051/0004-6361:200811296
- Zechmeister, M., Reiners, A., Amado, P. J., et al. 2018, *A&A*, 609, A12, doi: 10.1051/0004-6361/201731483
- Zechmeister, M., Dreizler, S., Ribas, I., et al. 2019, *A&A*, 627, A49, doi: 10.1051/0004-6361/201935460

Appendix 1 Radial Velocity Measurements

Table 3: RVs for Ross 508.

BJD (-2450000)	RV (ms^{-1})	Uncertainty (ms^{-1})
8540.101484	-3.40	2.50
8565.084859	-2.30	2.43
8623.965979	-5.06	4.36
8623.971075	-7.11	2.71
8623.984402	0.27	3.14
8623.988127	-7.98	3.13
8656.804690	1.10	2.37
8736.724410	4.01	3.80
9004.939392	7.70	2.23
9004.946975	2.95	2.24
9005.972814	7.39	2.99
9005.980543	-1.40	2.69
9005.988855	3.97	2.84
9006.960442	-3.99	2.35
9006.967935	5.54	2.42
9007.882653	-2.05	2.30
9007.890162	2.98	2.30
9010.965542	-0.56	2.21
9010.973732	2.87	2.32
9011.918730	-0.84	2.22
9012.987404	-7.40	3.00
9012.993618	1.11	2.89
9014.952306	2.15	2.39
9014.959983	8.99	2.31
9017.952195	0.52	2.35
9017.959774	-3.71	2.43
9029.955337	4.42	2.25
9029.962978	0.18	2.22
9030.952815	-2.23	2.32
9030.960649	-0.90	2.30
9031.947822	-6.02	2.62
9031.955839	-2.77	2.44
9032.950886	-4.22	2.26
9032.958518	-8.38	2.30
9033.958650	-4.60	2.21
9033.966256	-2.75	2.13
9034.876530	-0.86	2.24
9034.884052	-0.05	2.18
9035.952939	2.06	2.39
9035.960628	0.34	2.31
9036.946364	6.51	2.33
9036.953908	7.24	2.31
9037.954089	4.63	2.53
9037.961776	0.57	2.47
9052.760439	1.09	2.58

(Continued)

BJD (-2450000)	RV (ms^{-1})	Uncertainty (ms^{-1})
9052.767841	-0.41	2.48
9054.740438	-6.13	2.58
9054.747908	-2.84	2.56
9055.737313	-1.26	2.79
9055.746024	-0.83	2.84
9062.738505	-7.60	2.64
9062.746918	-1.06	2.63
9064.753007	-6.63	2.57
9065.730471	-3.30	2.60
9065.738626	1.92	2.60
9068.828720	7.37	3.48
9068.835744	4.97	3.17
9301.100420	-13.15	12.78
9301.924685	-4.96	3.52
9301.931132	-7.24	4.16
9305.012038	3.51	2.55
9305.021274	0.05	2.44
9321.988167	0.33	3.39
9321.991843	6.56	3.47
9329.979601	7.24	3.54
9329.984625	3.49	3.38
9335.998818	1.56	2.38
9336.006043	-0.96	2.38
9336.903887	1.66	2.31
9336.914754	1.94	2.26
9352.843703	0.65	2.73
9352.850681	1.97	2.70
9353.824596	-5.58	2.71
9353.829970	-4.19	2.77
9354.825976	-0.43	2.59
9354.832940	-2.78	2.60
9367.811663	1.07	2.90
9367.817009	-4.90	2.68
9368.804957	-2.86	2.76
9368.809560	0.26	2.74
9369.812588	2.78	2.80
9369.817475	1.25	2.81
9370.812156	1.10	2.47
9370.818195	7.52	2.55
9371.828379	8.15	2.36
9371.834659	2.45	2.42
9372.819000	2.06	2.48
9372.825454	-2.33	2.42
9410.740034	0.57	3.07
9410.743733	-4.85	3.02
9411.743618	-3.48	3.61
9411.747263	2.08	3.62

(Continued)

BJD (-2450000)	RV (ms^{-1})	Uncertainty (ms^{-1})
9452.777252	8.36	3.56
9452.780933	2.07	3.63
9453.799319	4.47	3.62
9453.803015	9.77	3.61
9455.725685	4.62	3.00
9455.731175	13.25	3.02
9468.728240	9.62	3.12
9468.733409	12.50	3.08
9486.714323	1.74	3.52
9486.719672	4.35	3.13

Appendix 2 Additional Figures

Figures 8 through 13 show the best-fit orbital solutions and the corner plots. Each pair of figures corresponds to Model A1, A2, and B2, respectively.

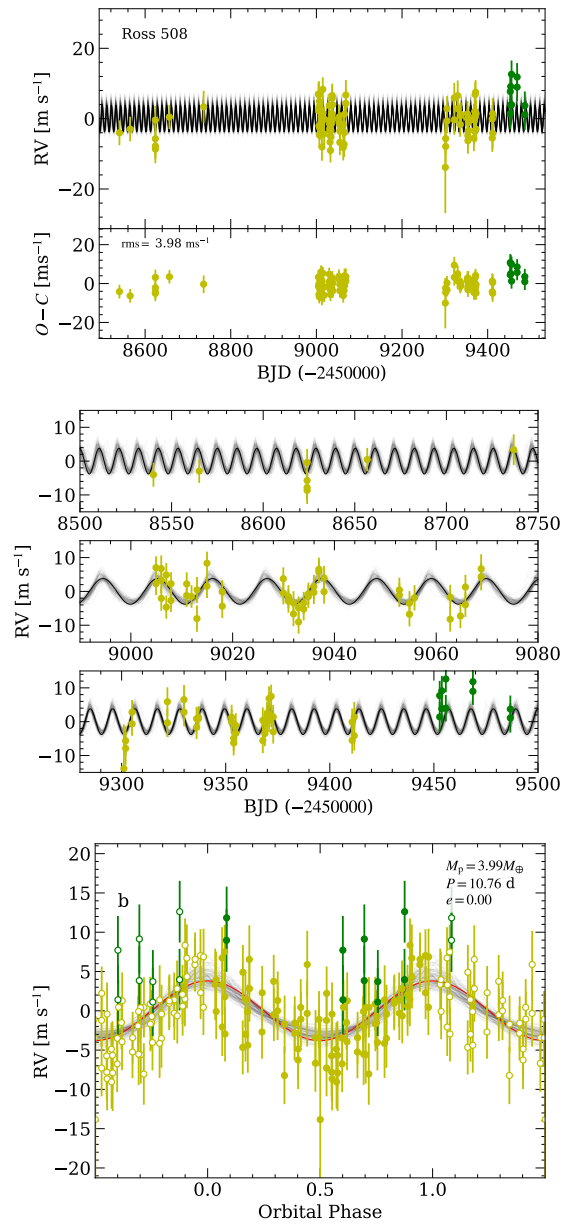


Fig. 8. Observed RVs and best-fit RV model of Model A1. See caption to Figure 3 for details.

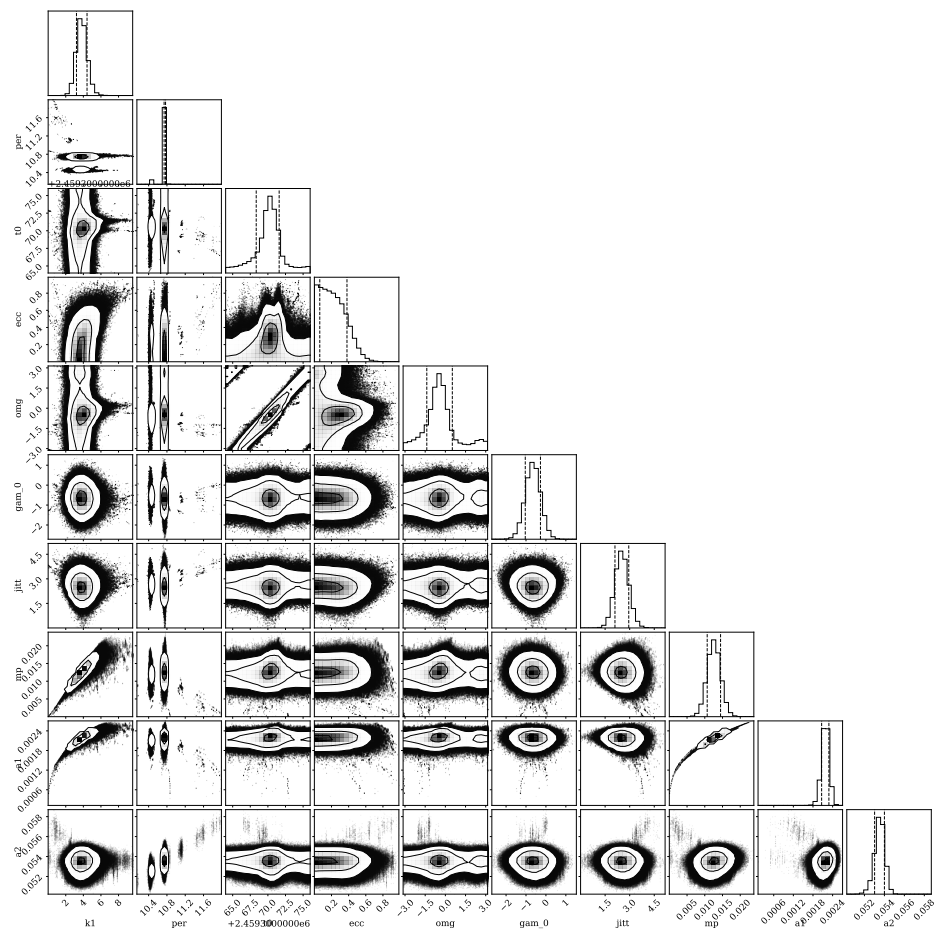


Fig. 9. Corner plot of Model A1.

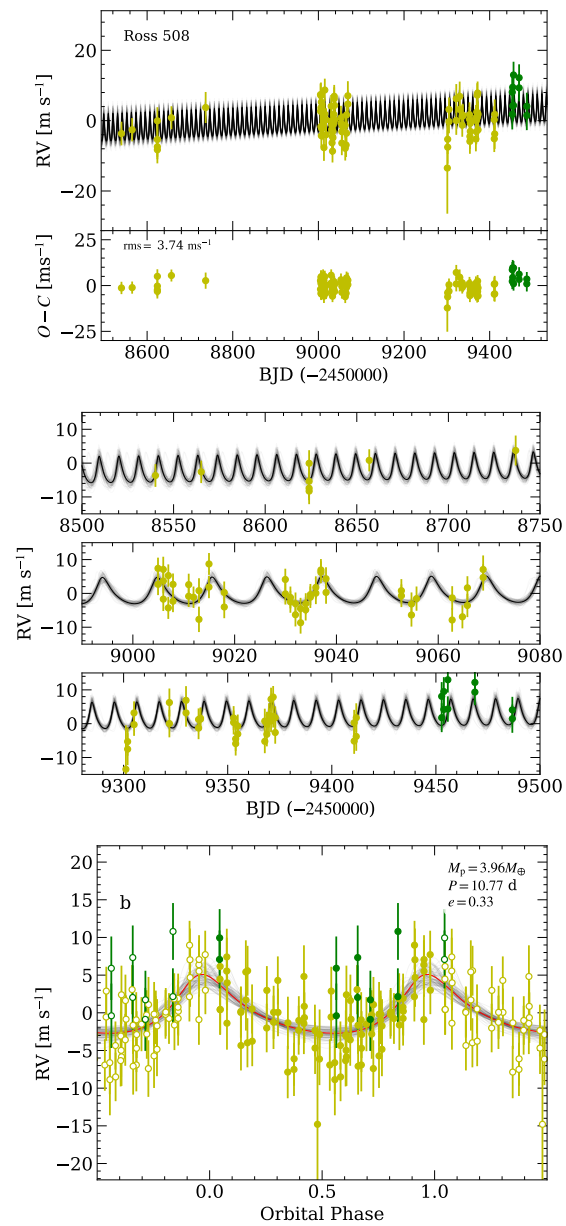


Fig. 10. Observed RVs and best-fit RV model of Model A2. See caption to Figure 3 for details.

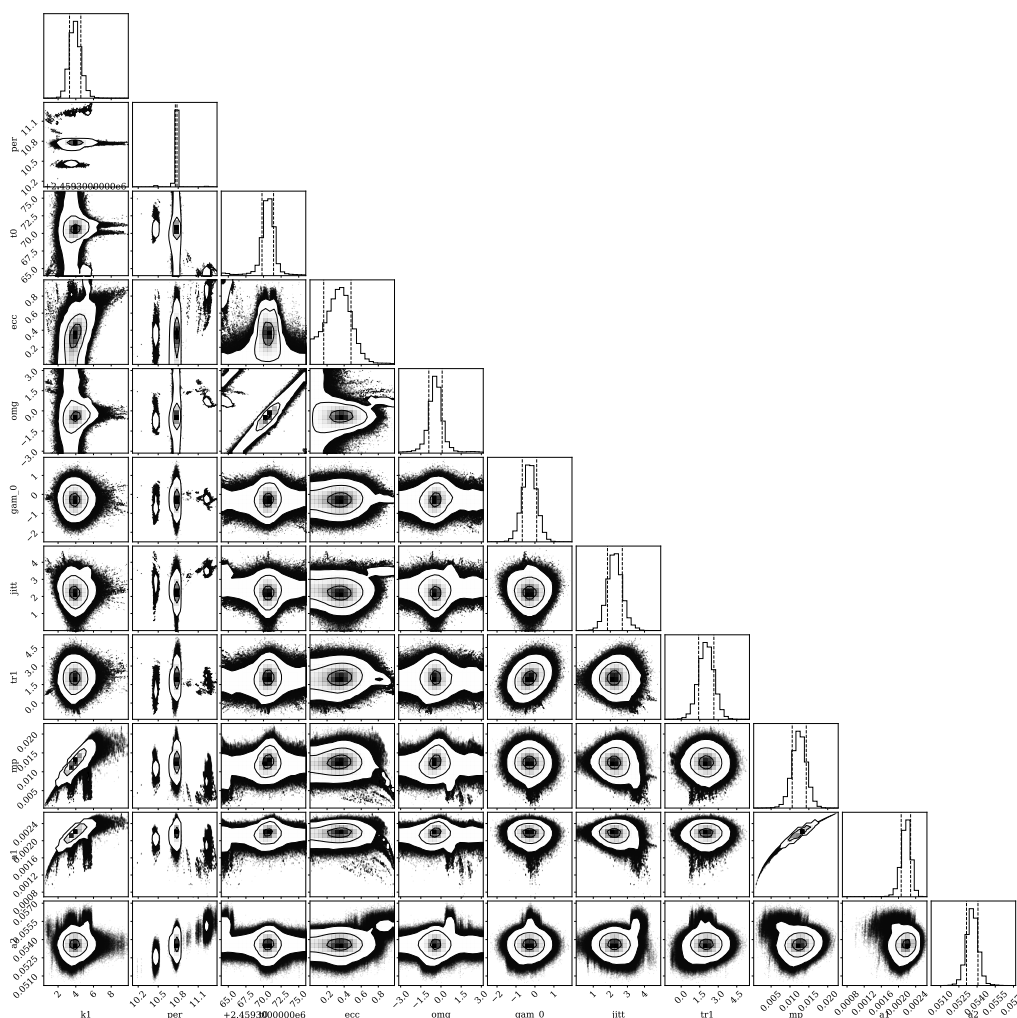


Fig. 11. Corner plot of Model A2.

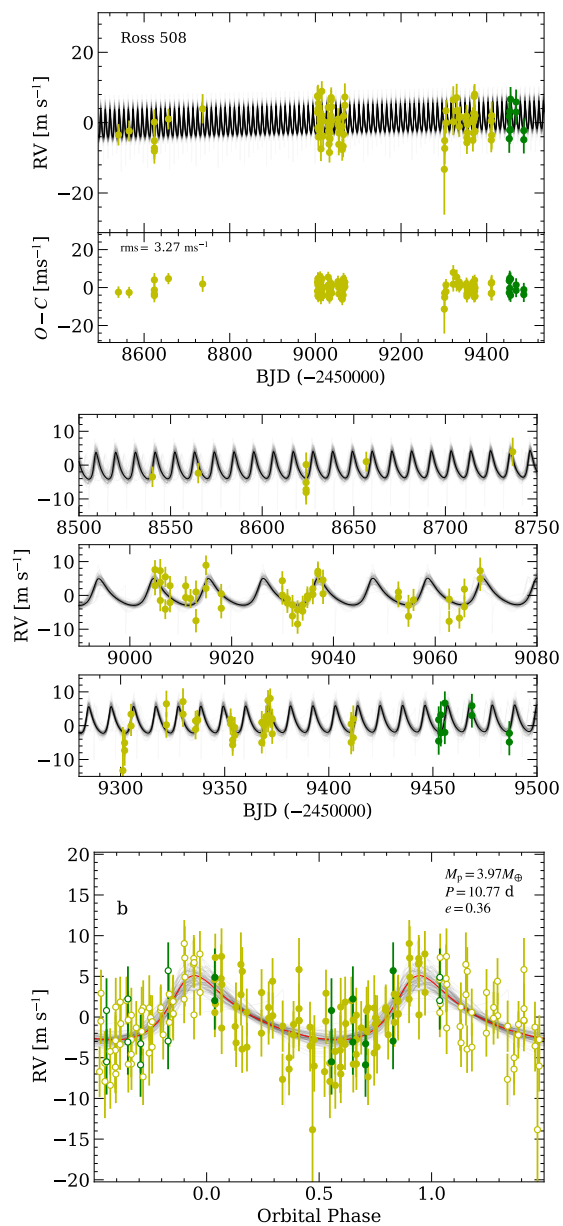


Fig. 12. Observed RVs and best-fit RV model of Model B2. See caption to Figure 3 for details.

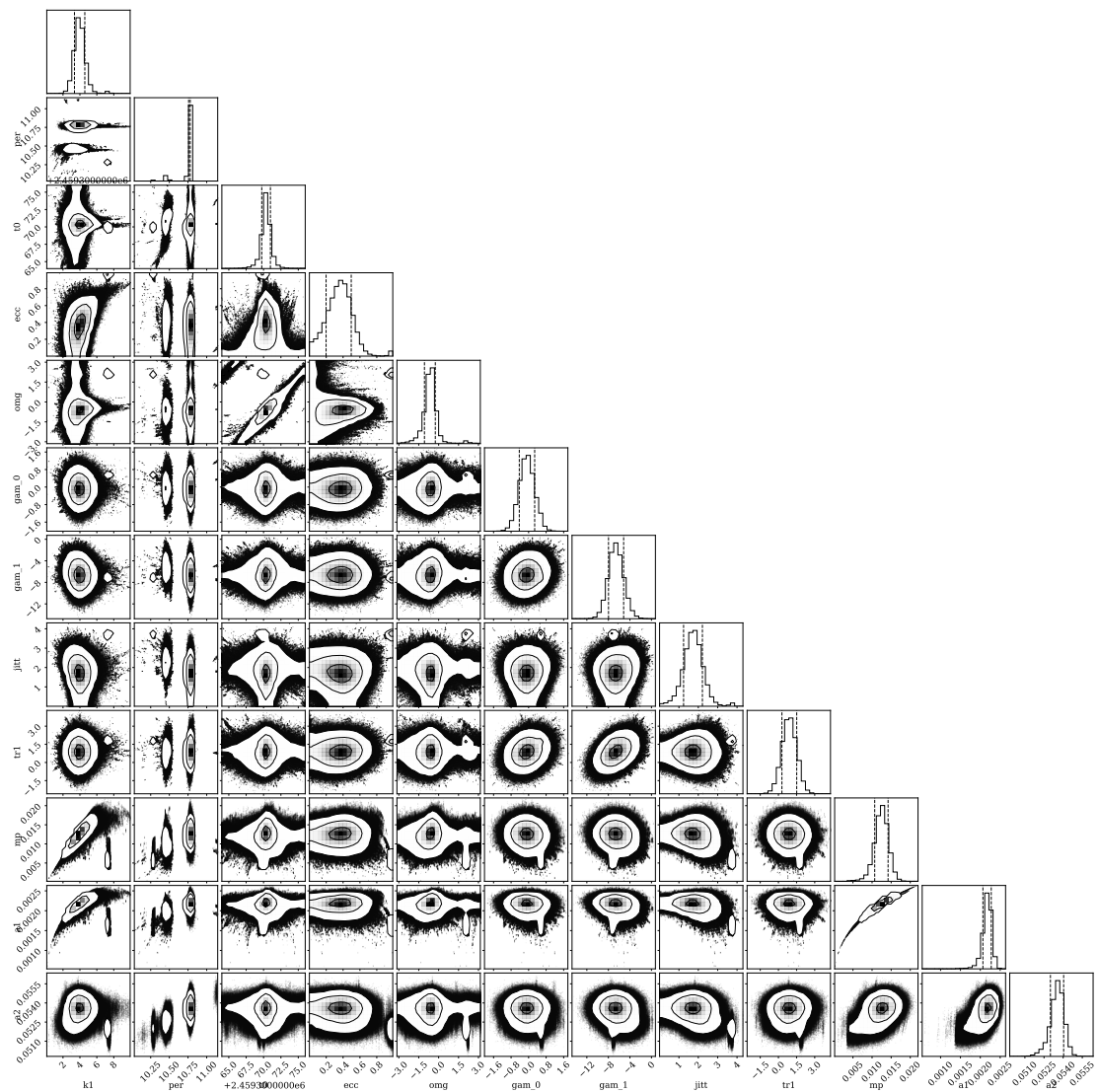


Fig. 13. Corner plot of Model B2.